Post-failure behavior of long wires under dynamic pulse buckling

Bergson S. Matias[1], Jonas Aguiar Jr.[1], Evandro Parente Jr.[1], A. Macário C. de Melo[1], Fábio P. S. Mineiro[2],
Anderson B. Custódio[2]

[1]*Laboratório de Mecânica Computacional e Visualização (LMCV), Departamento de Engenharia Estrutural e
Construção Civil, Universidade Federal do Ceará*
Campus do Pici, Bloco 728, Fortaleza, 60440-900, Ceará, Brazil
bergson.sm@gmail.com, jonasaguiarj@hotmail.com, evandro@ufc.br, macario@ufc.br
[2]*Centro de Pesquisas Leopoldo Américo Miguez de Mello (CENPES), Petrobrás*
*Av. Horácio Macedo, 950, Cidade Universitária da Universidade Federal do Rio de Janeiro, Rio de Janeiro,
21941-915, Brazil*
fabiomineiro@petrobras.com.br, andersonbc@petrobras.com.br

Abstract. The phenomenon of dynamic pulse buckling, which can appear with the failure of long slender structures under tension, as offshore structures such as risers, has drawn the attention of the interest of researchers due to accidents and the damage they can cause to the environment. The risers connect floating units to flowlines and other equipment on the seabed and are used for drilling and exploration of oil and gas. Experimental and numerical researches have been conducted in reduced wire models to study post-failure behavior, mainly after the compressive elastic unloading wave reaches the fixed end, being reflected and giving rise to a buckling located near this end. This work addresses the finite element modeling and simulation of dynamic pulse buckling in wire failure tests. An elastoplastic model with linear hardening is adopted for the material behavior. Explicit and implicit integration algorithms are used for nonlinear dynamic analysis considering 2D and 3D beam elements with large displacements and strains. The effects of the finite element type, mesh discretization, integration algorithm, geometric imperfections, numerical damping, wire length, and time step in the post-failure behavior are assessed and the implications of these results for the simulation of post-failure analysis of marine risers are discussed.

Keywords: Dynamic Buckling, Nonlinear Dynamics, Finite Element Analysis.

1 Introduction

Long slender structures under tension, e.g., offshore structures such as risers, are subject to dynamic pulse buckling. This phenomenon has drawn the attention of researches due to accidents that have occurred and the related damages to the environment [1]. These failures can be amplified by the great connectivity between risers, floating units, flowlines and equipaments on the seabed. Although the conditions are different, experimental and numerical researches have been conducted in reduced wire models to study post-failure behavior, mainly after the compressive elastic unloading wave reaches the fixed end, being reflected and giving rise to a buckling located near this end.

Paredes *et al.* [2] investigated the phenomenon of dynamic pulse buckling, numerically and experimentally, in a set of thin steel wires by pulling them until fracture. Depending on the slenderness, the wire develops an helical buckling pattern. By following this line of reasoning, this work aims to investigate the sensibility of some numerical parameters of a circular wire subjected to a sudden recoil and experiencing a dynamic pulse buckling.

2 Dynamic pulse buckling

The dynamic pulse buckling is characterized by a single pulse defined by its amplitude, shape and duration [3]. It fits the mathematical definition of dynamic response induced by time-varying parametric loading [3]. For slender bars under intense loads, the deformation can reach large amplitudes with dynamic buckling modes of orders much larger than the static mode [3]. The unavoidable imperfections, mainly from geometric nature, are

responsible for initial bending. The structure can present permanent deformations if there is a plastic response or a snap-through to a post-buckling state of large deformations, or it can recover its initial configuration [3].

While in static analysis the focus is on determining the critical load for the fundamental buckling mode, in dynamic pulse buckling, the buckling mode itself depends on the amplitude specified for the load, an inversion in the analysis process that must be recognized for the good understanding of dynamic pulse buckling [3].

Experimental tensile tests on thin bars and long wires until the rupture induced in one of the extremities have been revealed three phases after the failure [2–5]. The last work is explored here. In Phase-I, a compressive elastic unloading wave propagates in direction to fixed end with speed $c = \sqrt{E/\rho}$ (E: Young modulus; ρ: material density). The side of the wire behind the wave front is stress free and moves in the same direction with speed $\nu = c\sigma_f/E$ (σ_f: ultimate strength). The phenomenon is described by the one-dimensional wave equation [6]. Phase-II starts with the impact of the long wire against the rigid end when the wave front reaches it. A new compressive wave is reflected. The uniform compressive state remains only close to the wave front and gives way to bending with the increasing of the imperfections. Phase-III is characterized by the reflection of a dispersive bending wave due to the deformed shape of the wire.

When the compression unload wave reaches the opposite fixed end, at the final of Phase-I, the phenomenon of dynamic pulse buckling can start there and is similar to the impact of a tension-free bar against a rigid wall. Theoretical discussions can be developed considering a supported column, subjected to a compression load P and with an initial imperfection $y_0(x)$ as done in [3, 4]. The bar deformation is controlled such the displacement $y(x)$ starts only when the full load P is applied. An expression for the dimensionless displacement $w = y/r$, where r is the radius of gyration of the cross section, can be obtained using Fourier series [3, 4]

$$w(\xi, \tau) = \sum_{n=1}^{\infty} g_n(\tau) sen(\eta \xi) \quad g_n(\tau) = \frac{a_n}{1 - \eta^2} \left[\begin{matrix} \cos \\ \cosh \end{matrix} (p_n)\tau - 1 \right] \quad p_n = \eta |1 - \eta^2|^{\frac{1}{2}} \quad (1)$$

The nature of the solution is governed by the wave number $\eta = n\pi/l$, which is trigonometric for $\eta > 1$ (displacement are bounded). The form is hyperbolic for $\eta < 1$, i.e., for ($P > P_1 = \pi^2 EI/L^2$, and the solutions grow exponentially with time. The frontier between solutions is defined by the mode number $n = kL/\pi$ corresponding to a mode with the wavelength of the static buckling mode for load P. The analysis of the amplification function, defined as the ratio between $g_n(\tau)$ and the Fourier coefficients a_n of the initial displacement, suggests for the most amplified mode the wave number $n_p = 1/\sqrt{2}$, also called preferred mode of buckling [5], with the wavelength near $8.88r\sqrt{\varepsilon}$, where $\varepsilon = P/(EA)$.

3   Parametric study

The parametric study conducted in this work was performed by using Abaqus software package [7]. In order to simulate the experimental test of the wire until rupture, it was initially applied a static load from zero to a P force (corresponding to the fracture force). After reach this value, the force P is suddenly removed by deactivating the initial conditions and a dynamic analysis is initiated. Figure 1 outlines this process.
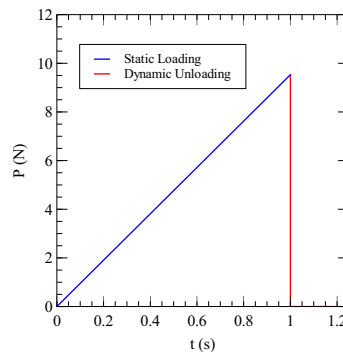

Figure 1. Loading and unloading process

For a more complete understanding of the phenomenon, 2D and 3D models were analyzed. Regarding the material, the elastic properties were defined as E = 200 GPa and ν = 0.3. Also, a Jonhson-Cook hardening constitutive model was used with the following parameters: A = 590 MPa, B = 1400 GPa and n = 1.0 [7]. Density used was ρ = 8000 kg/m^3.

The nomenclature adopted to identify these models follows an alphanumeric sequence: MABCDE-XY. Where MA indicates the dimension of the model (2D or 3D), BC indicates the main objective of the model (Nu for numerical and En for experimental comparisons), DE indicates the integration method (Im for implicit and Ex for explicit) and XY indicates the numerical order of the model.

For 2D models, linear (B21) and quadratic (B22) Timoshenko beam elements were adopted. In addition, a hybrid formulation elements were tested (B21H and B22H). Geometric imperfections were applied to the wire model, using the Abaqus [7] Spline tool, giving the wire a sinusoidal shape. The mesh sensitivity was studied, attributing two types of refinements to the wire: (1) uniform with 400, 200 and 100 elements and (2) biased non-uniform 1 with smaller elements at the fixed end. In addition, the numerical damping parameters and the time integration algorithms (implicit HHT method and explicit central difference method) were studied. Table 1 shows a summary of the 2D models assessed.

Table 1. 2D models studied

| Title | Element type | N. of elements | Imperfection | | Num. damping |
			a_0	μ (mm)	
M2NuIm-1	B22	400	-	-	$\alpha = -0.333$
M2NuIm-4	B22	400	-	-	$\alpha = -0.050$
M2NuIm-5	B22	400	-	-	$\alpha = -0.200$
M2NuIm-10	B21	400	-	-	$\alpha = -0.333$
M2NuIm-11	B21H	400	-	-	$\alpha = -0.333$
M2NuIm-12	B22H	400	-	-	$\alpha = -0.333$
M2NuIm-23	B22	554 (N.U.; 2x)[1]	-	-	$\alpha = -0.333$
M2NuIm-24	B22	805 (N.U.; 5x)	-	-	$\alpha = -0.333$
M2NuIm-25	B22	1023 (N.U.; 10x)	-	-	$\alpha = -0.333$
M2NuIm-31	B22	100	-	-	$\alpha = -0.333$
M2NuIm-32	B22	200	-	-	$\alpha = -0.333$
M2NuEx-3	B22	400	-	-	$\beta_1 = 0.060$
M2NuEx-26	B22	554 (N.U.; 2x)	-	-	$\beta_1 = 0.060$
M2NuEx-27	B22	805 (N.U.; 5x)	-	-	$\beta_1 = 0.060$
M2NuEx-28	B22	1023 (N.U.; 10x)	-	-	$\beta_1 = 0.060$
M2NuEx-29	B22	400	-	-	$\beta_1 = 0.120$
M2NuEx-30	B22	400	-	-	$\beta_1 = 0.240$
M2NuEx-33	B22	100	-	-	$\beta_1 = 0.060$
M2NuEx-34	B22	200	-	-	$\beta_1 = 0.060$
M2EnIm-17	B22	400	$0.2d_0$	60	$\alpha = -0.333$
M2EnIm-18	B22	400	$0.4d_0$	60	$\alpha = -0.333$
M2EnIm-19	B22	400	$0.2d_0$	30	$\alpha = -0.333$

[1]Biased non-uniform

For 3D models, a quadratic beam element (B32) with similar characteristics to the 2D models was used. The time integration algorithms and geometric imperfections were investigated. In this case, geometric imperfections with helical and random shapes were studied. In addition, in order to obtain results closer to Paredes *et al.* experimental test [2], the effect of gravity and the presence of a barrier at the fixed end were studied. This boundary condition is important to reproduce the testing machine fixing jaws that prevent the wire moving beyond the fixed end. This barrier was visually verified in the experimental test equipment. Table 2 shows a summary of the 3D models studied.

A general scheme of the 2D and 3D models imperfections is shown in Figure 2. Figure 2(a) shows that the imperfections adopted for 2D models are function of two geometric parameters, a half wavelength μ and a

Table 2. 3D models studied

| Title | N. of elements | Imperfection | | Additional |
		Type	a_0	
M3NuEx-36	400	-	-	Gravity
M3NuIm-39	400	-	-	-
M3NuIm-40	400	-	-	Gravity
M3EnIm-42	300	Helical	$0.2d_0$	-
M3EnIm-44	300	Helical	$0.3d_0$	-
M3EnIm-45	300	Helical	$0.4d_0$	-
M3EnIm-46	300	Helical	$0.5d_0$	-
M3EnIm-47	300	Random	$0.2d_0$	-
M3EnIm-48	300	Random	$0.3d_0$	-
M3EnIm-49	300	Random	$0.4d_0$	-
M3EnIm-50	300	Random	$0.5d_0$	-
M3EnIm-52	300	Helical	$0.5d_0$	Barrier
M3EnIm-56	300	Helical	$0.2d_0$	Barrier
M3EnIm-57	400	Helical	$0.5d_0$	Barrier

amplitude a_0. Similarly as shown in Figure 2(b), the 3D helical and random imperfections are function of a half wavelength μ and a amplitude a_0. However, for 3D helical imperfections, a more complex function was needed.

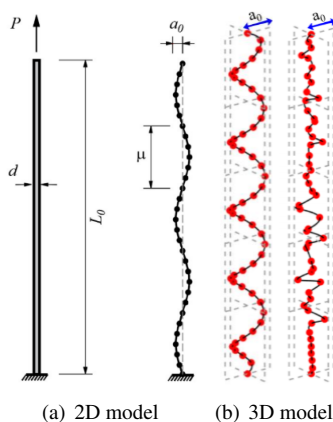(a) 2D model   (b) 3D model

Figure 2. Imperfections adopted in 2D and 3D models

4   Results and discussions

The results obtained for the parametric study can be arranged in three main groups. The first group corresponds to the Phase-I behavior. In all models (including 2D or 3D), the compressive elastic unloading wave is well represented in Phase-I. However, it has been noted that, for the implicit algorithm, there is a small gap in the path of the wave thought the wire. This behavior is depicted in Figure 3(b). Furthermore, also for the implicit algorithm, it is possible to verify the appearance of some instability.

After first reflection, during Phase-II, the instability of the compressive wave increases, as shown in Figures 4(b) and 4(c). Specially in Figure 4(c) it is possible to verify (at 0.16 ms) a clear appearance of spurious vibrations. At this point, Phase-III starts and it can be observed a second group of results: the behavior of the wire with the inclusion of bending and torsion moments.

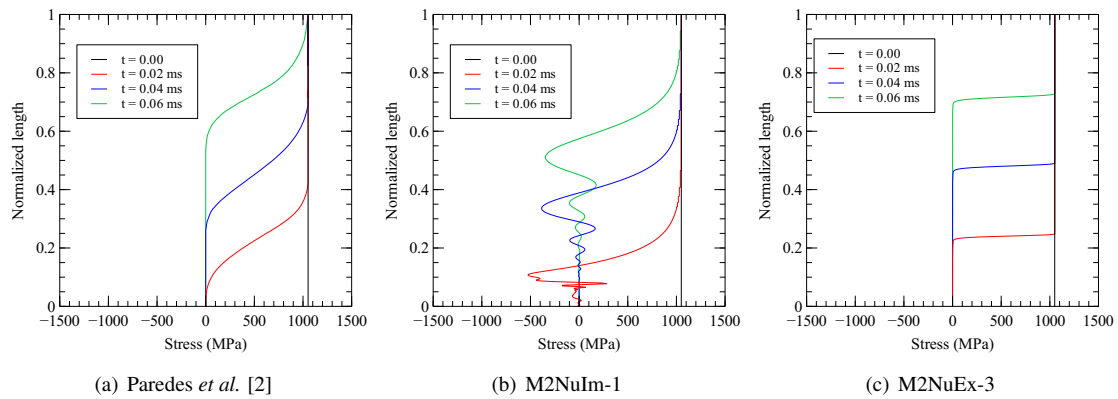To present the main observations about the behavior of the wire at Phase-III, Figure 5 shows the vertical and

(a) Paredes *et al.* [2]   (b) M2NuIm-1   (c) M2NuEx-3

Figure 3. Compression wave before first reflection

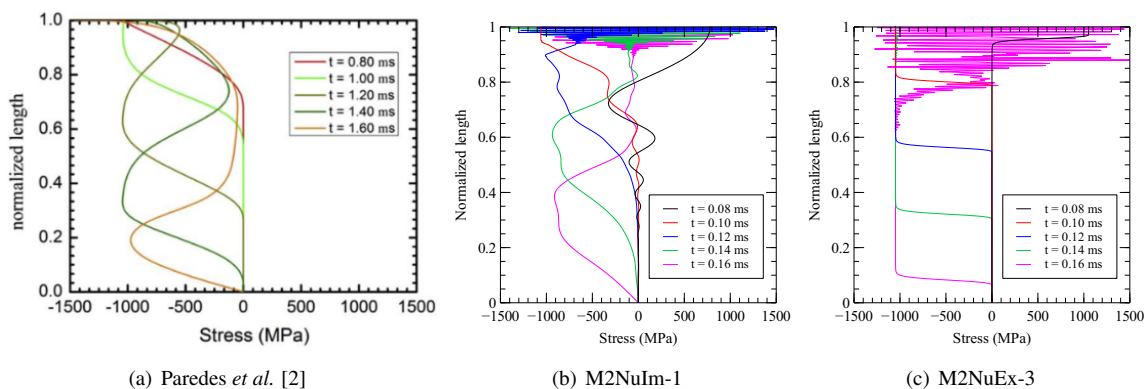(a) Paredes *et al.* [2]   (b) M2NuIm-1   (c) M2NuEx-3

Figure 4. Compression wave after first reflection

the moment reactions in the fixed end during the first 0.80 ms for two models without geometric imperfections (M2NuIm-1 and M2NuEx-3).

As Figure 5 illustrates, there is a difference between Implicit (Figure 5(b)) and Explicit (Figure 5(c)) algorithm results. For nearly all of the Explicit models, Phase-III presents a vibratory behavior. On the other hand, depending on the numerical damping parameter, the Implicit models present a more smooth vibration. Nevertheless, for all 2D models without imperfections, it was not possible to find a pattern for the vibration at Phase-III.

In terms of envelopes, the most of the models present a range varying between -10 N and 10 N for the vertical reaction and a range between -0.3 N·mm and 0.3 N·mm. This indicates a controlled sensibility for the results. From a qualitative viewpoint, the absence of initial imperfections in 2D models is not necessarily damaging for global analyses.

When initial imperfections are placed in the models, it is observed more well-established outcomes. Figure 6 illustrates this affirmation with the reaction results for M2EnIm-17, M2EnIm-18 and M2EnIm-19 models, where M2EnIm-17 has the same amplitude a_0 as M2EnIm-19, but with different half wavelength μ, and M2EnIm-17 has the same half wavelength μ as M2EnIm-18, but with different amplitude a_0 (all with initial geometric imperfections). Besides this less vibratory behavior, it can be noticed a well-defined pattern for the reactions at Phase-III. These results indicate that real imperfections are necessary for good analyses.

For 3D models, the main results show that the consideration of geometric imperfections may lead to a more flexible behavior, as illustrated in Figure 7. All models which considered some type of imperfection present the deformed configuration passing the lower threshold. This limit corresponds to the physical barrier existing at the fixed end.

Model M3EnIm-44 has a imperfection with a helical shape. The deformed configuration showed in Figure 7 presents also a helical shape at Phase-III. Its distribution at XY plane is almost circular. It was observed, in 3D models without imperfections, a more planar behavior at Phase-III. Paredes *et al.* [2] have performed a set of experimental simulations. Figure 8 shows a comparison between the results obtained by [2] and the model M3EnIm-44. It can be noted that the experimental result presents more waves.

Aiming to approximate the numerical results with the experimental results obtained by [2], it was proposed the addition of a barrier in the fixed end. The results are presented in Figure 9. It can be observed that the presence
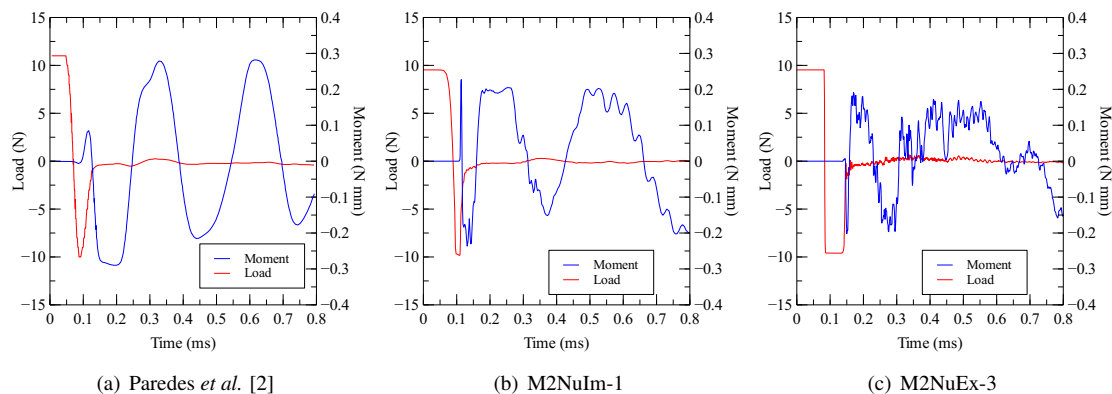
| (a) Paredes *et al.* [2] | (b) M2NuIm-1 | (c) M2NuEx-3 |

Figure 5. Vertical and moment reactions behavior for 2D models without geometric imperfections

| (a) M2EnIm-17 | (b) M2EnIm-18 | (c) M2EnIm-19 |
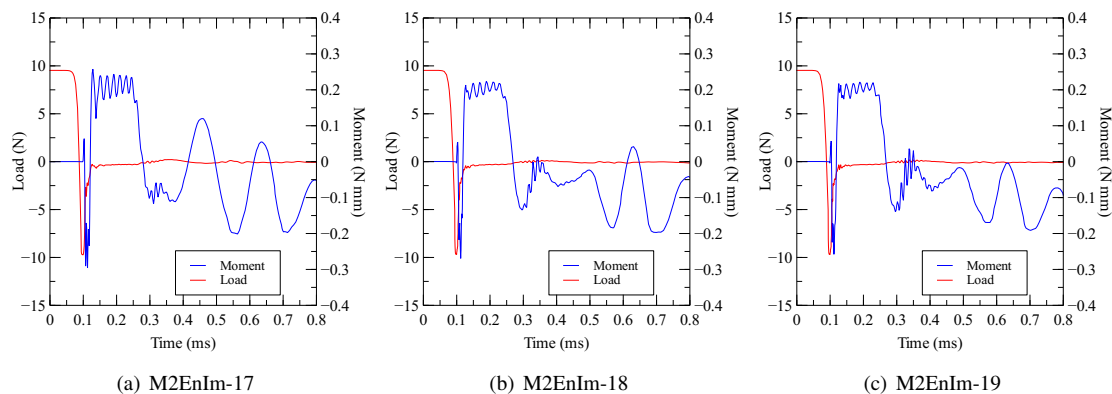
Figure 6. Vertical and moment reactions behavior for 2D models with geometric imperfections

| (a) XYZ projection | (b) XY projection | (c) XZ projection |
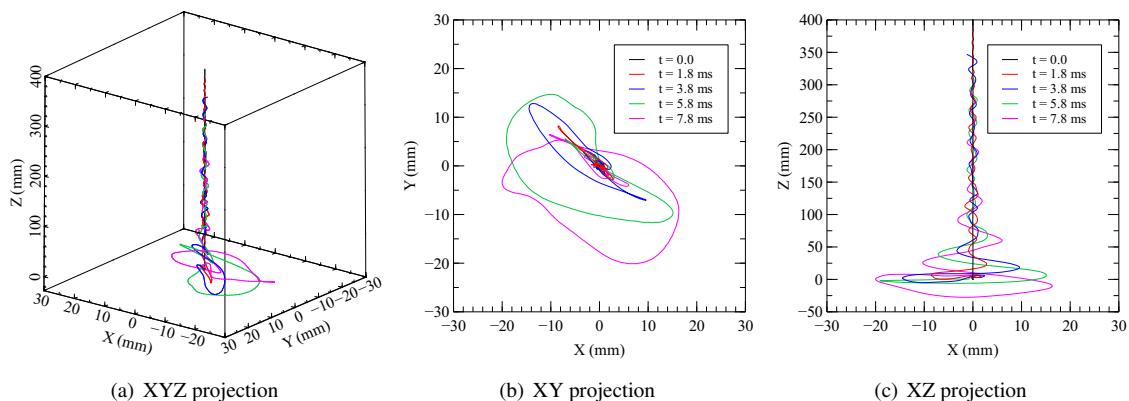
Figure 7. 3D deformed configuration of M3EnIm-44 model

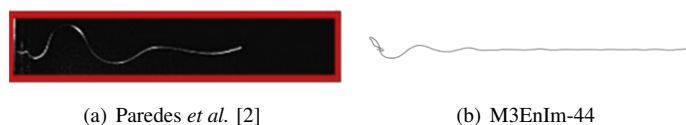| (a) Paredes *et al.* [2] | (b) M3EnIm-44 |

Figure 8. Projection of deformed at time 4.4 ms

of this barrier was necessary to achieve reasonable results. Figure 10 shows the deformed configuration of the M2EnIm-57 model.
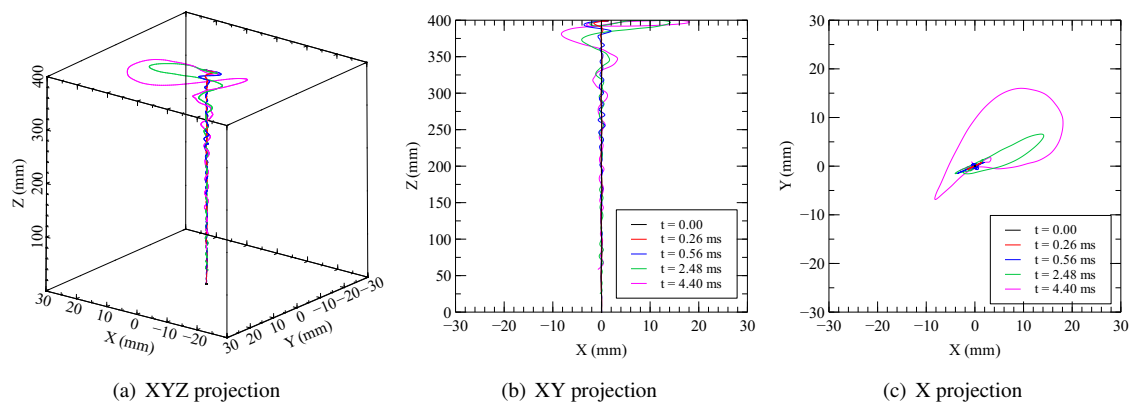

| (a) XYZ projection | (b) XY projection | (c) X projection |

Figure 9. 3D deformed configuration of M3EnIm-57 model

| (a) Paredes *et al.* [2] | (b) M3EnIm-57 |

Figure 10. Projection of deformed at time 4.4 ms

5 Conclusions

Some important aspects of dynamic pulse buckling and wave propagation in steel wires are studied in order to assess the post-failure behavior of marine risers. It was observed a great sensibility in the results due to presence of initial geometric imperfections. Furthermore, this study helps to understanding the three phases of the dynamic pulse buckling in a wire and which are its importance to the analysis. With respect to the numerical parameters, the Implicit algorithm presented best performance and results more smooth, mainly at Phase-III.

Authorship statement. The authors hereby confirm that they are the sole liable persons responsible for the authorship of this work, and that all material that has been herein included as part of the present paper is either the property (and authorship) of the authors, or has the permission of the owners to be included here.

References

[1] Petronoticias, 2020. Petrobrás sofre novo rompimento de riser flexível no fpso angra dos reis. *PetroNoticias*.
[2] Paredes, M., Wierzbicki, T., & Roth, C. C., 2015. Three dimensional, flexural-torsional dynamic buckling of long wires after tensile fracture and implications on deep water riser dynamics. *International Journal of Impact Engineering*, vol. 86, pp. 27–39.
[3] Lindberg, H. E. & Florence, A. L., 1983. *Dynamic Pulse Buckling: Theory and Experiment*. Defense Nuclear Agency.
[4] Lindberg, H. E., 1964. Buckling of a very thin cylindrical shell due to an impulsive pressure. *Journal of Applied Mechanics*, vol. 31, pp. 267–272.
[5] Lindberg, H. E., 2003. *Little Book of Dynamic Buckling*. Penn Valley: LCE Science.
[6] Rao, S., 2007. *Vibration of Continuous Systems*. Florida: John Wiley & Sons.
[7] Simulia, 2012. ABAQUS/Standard user's manual.